

Radiative transfer solution for rugged and heterogeneous scene observations

Christophe Miesch, Xavier Briottet, Yann H. Kerr, and François Cabot

A physical algorithm is developed to solve the radiative transfer problem in the solar reflective spectral domain. This new code, Advanced Modeling of the Atmospheric Radiative Transfer for Inhomogeneous Surfaces (AMARTIS), takes into account the relief, the spatial heterogeneity, and the bidirectional reflectances of ground surfaces. The resolution method consists of first identifying the irradiance and radiance components at ground and sensor levels and then modeling these components separately, the rationale being to find the optimal trade off between accuracy and computation times. The validity of the various assumptions introduced in the AMARTIS model are checked through comparisons with a reference Monte Carlo radiative transfer code for various ground scenes: flat ground with two surface types, a linear sand dune landscape, and an extreme mountainous configuration. The results show a divergence of less than 2% between the AMARTIS code and the Monte Carlo reference code for the total signals received at satellite level. In particular, it is demonstrated that the environmental and topographic effects are properly assessed by the AMARTIS model even for situations in which the effects become dominant. © 2000 Optical Society of America

OCIS codes: 010.1300, 280.0280.

1. Introduction

Solving the radiative transfer problem is an essential part of quantitative studies related to existing and new satellite missions that incorporate remote sensors. The relevance of remotely sensed data depends critically on the spectral bands chosen and on the calibration accuracy of the instruments. Optimizing instrument specifications for a given field or performing in-flight calibration of the sensors requires accurate evaluations of the radiance that reaches the instrument after its path through the atmosphere. For the solar-reflective spectral domain, radiative transfer codes such as 6S (Ref. 1) and MODTRAN (Ref. 2) have already been developed to provide a computational solution for calculating the

radiance that reaches a given sensor. However, most of these existing algorithms are able to deal only with flat and homogeneous ground surfaces. Several published results³⁻⁷ demonstrate that these assumptions are too rigorous for heterogeneous or rugged scenes. In a previous study,⁸ an overview analysis of such effects was presented in which a statistical Monte Carlo method was used to resolve topographic surface and atmospheric effects. Simulations of typical ground scenes were carried out, and the results show in particular the necessity for properly calculating the environmental and topographic effects on signal received by a remote sensor. Unfortunately, this kind of statistical simulation requires computation times that are prohibitively long for use on a routine basis.

The need for a fast computational model that is capable of topographic resolution led us to develop the method that we report here. Our method consists in analyzing separately the various radiative components that reach an airborne or a satelliteborne sensor bound on their physical origin. The irradiance components at ground level are identified before the upward radiance terms are treated. The various radiative components are then calculated separately by use of models derived principally from improved versions of the usual spatially resolved approaches (which originally dealt only with flat and homogeneous targets). Such a process implies the inevita-

C. Miesch (christophe.miesch@oncert.fr) and X. Briottet (Xavier.briottet@oncert.fr) are with the Département d'Optique Théorique et Appliquée, Office National d'Etudes et de Recherches Aéropatiales, 2 avenue E. Belin, 31400 Toulouse, France. Y. H. Kerr (yann.kerr@cesbio.cnes.fr) is with the Centre d'Etude Spatiale de la Biosphère, 18 avenue E. Belin, 31400 Toulouse, France. F. Cabot (francois.cabot@est.cnes.fr) is with the Centre National d'Etudes Spatiales, Qualité et Traitements des Images Satellitaires, 18 avenue E. Belin, 31400 Toulouse, France.

Received 13 December 1999; revised manuscript received 29 August 2000.

0003-6935/00/366830-17\$15.00/0

© 2000 Optical Society of America

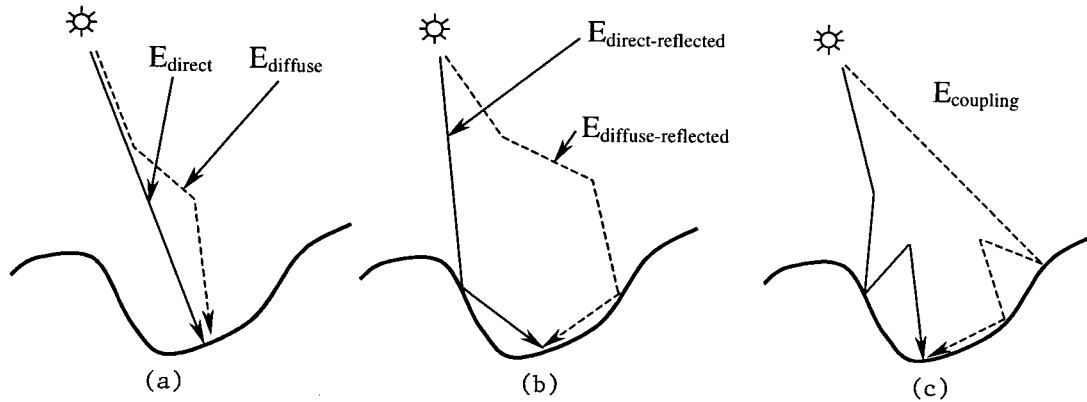


Fig. 1. Irradiance components at ground level.

ble introduction of simplifying assumptions, and for this reason it is necessary to check their validity, that is, whether they produce only negligible bias on the results. To this end, three simulations are performed for various atmospheric and ground conditions. Results given by our code, Advanced Modeling of the Atmospheric Radiative Transfer for Inhomogeneous Surfaces (AMARTIS), are checked against the output of a Monte Carlo resolution method,⁸ which is taken as the reference.

2. Signal Modeling

The radiative transfer code presented here deals with monochromatic simulations of the radiance that reaches a given sensor that is remote from the Earth's surface. A scene at ground level entirely described by a digital elevation model and an associated reflectance map that characterizes the directional behavior of each element of the ground surface are assumed, as is a plane-parallel atmosphere divided into horizontally homogeneous layers that are characterized by extinction, scattering, and absorption coefficients for both molecules and aerosols. The Earth-atmosphere system is assumed to be conservative, which is equivalent to assuming a periodicity of the scene along both horizontal axes. The largest assumption introduced in our model is that gaseous absorption can be considered separately from other atmospheric phenomena (e.g., scattering). This assumption, used in most codes, is particularly important for multispectral simulations because gaseous absorption varies strongly with wavelength, which is not the case for scattering effects. Thus it is more efficient to compute the spectral dependence of the scattering effects and that of the gaseous absorption separately, with different-sized spectral steps for each (the absorption computation requires smaller intervals than the scattering simulation), before integrating the signal over the spectral band of interest.

A. Irradiance at Ground Level

The signal coming from the Sun and reaching the ground can travel along different paths. Five main

types of path can be identified. The most obvious interactions are those of direct and diffuse components [Fig. 1(a)]. Over rugged terrain, a photon may be reflected by neighboring elements in the scene before it reaches the target [Fig. 1(b)]. These photons contribute to what we call the adjacency component. Finally, the Earth-atmosphere coupling irradiance term is used for photons that have been subjected to multiple reflections and scatterings [Fig. 1(c)] before reaching the surface. This term is also called the environmental component. The total irradiance that reaches a given elementary surface at ground level is then given by the sum of these five components:

$$E_{\text{direct}} = E_{\text{direct}} + E_{\text{diffuse}} + E_{\text{coupling}} + E_{\text{direct-reflected}} + E_{\text{diffuse-reflected}}. \quad (1)$$

Direct irradiance is generally the more dominant. It is also the easiest to model. Because of the relief, however, it is necessary to take into account possible blocking by the neighborhood (shadow), which would make the direct component zero. This shadowing effect can be taken into account by use of a binary mask, $o(P, \theta_s, \phi_s)$, set to zero if point P of ground model G (which is a digital elevation model in the AMARTIS code) is in the shadow for the solar incidence of (θ_s, ϕ_s) and is 1 otherwise. Note that θ designates the zenith angle of a given direction, whereas ϕ is the azimuth angle of this direction. The direct irradiance that reaches P is then

$$E_{\text{direct}}(P) = E_{\text{TOA}} o(P, \theta_s, \phi_s) \langle \hat{N}(P) \cdot \hat{n}_s \rangle \times \exp[-\tau^\downarrow(P)/\mu_s] T_g^\downarrow(P, \theta_s), \quad (2)$$

where E_{TOA} is the solar top-of-atmosphere irradiance; $\hat{N}(P)$ is a unit vector orthogonal to the slope of ground model G at P; \hat{n}_s is a unit vector pointed toward the Sun; $\tau^\downarrow(P)$ is the total atmospheric optical thickness of the vertical path above P (without gaseous absorption); and $\mu_s = \cos(\theta_s)$ and $T_g^\downarrow(P, \theta_s)$ is the gaseous transmission of the path from the Sun to P. The angle brackets indicate a vector dot product.

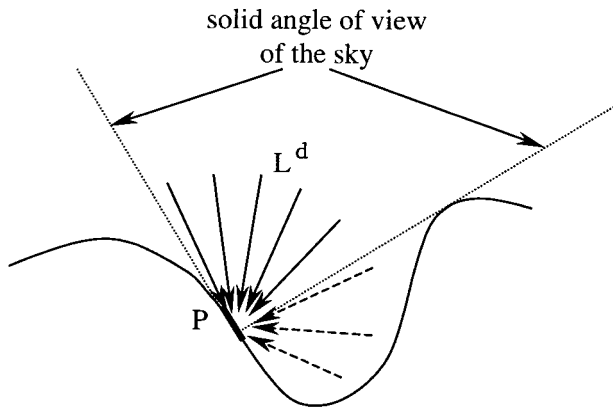


Fig. 2. Diffuse sky radiance incident upon a rugged terrain.

Integrating sky radiances over the hemisphere yield the diffuse irradiance. These radiances are calculated in our model for flat and homogeneous ground by use of the Gauss–Seidel successive-order resolution method.⁹ Over flat terrain, the integration of the sky radiances is given by

$$E_{\text{diffuse flat ground}}(M) = T_g^\downarrow(M, \theta_s) \times \iint_{\Omega=2\pi} L^d(z_M, \theta, \phi) \cos \theta d\omega, \quad (3)$$

where $L^d(z_M, \theta, \phi)$ is the sky radiance that is incident in direction (θ, ϕ) at altitude z_M of point M. Note here that the gaseous transmission is applied after integration of the diffuse sky radiance, as a result of the uncoupling of the gaseous absorption from the other phenomena. For a rugged surface we consider the same diffuse sky radiance distribution computed by the Gauss–Seidel code for the flat surface. However, for a sloped surface the integration needs to be carried out in the local reference system of the ground point that is being considered. Moreover, as Fig. 2 illustrates, the effect of the neighboring relief has to be taken into account. In practice, the integration of the incident diffuse signal is made according to the following rules: If the incident direction is inside the solid angle of view of the sky, the corresponding radiance is integrated as is; if the incident direction is outside the direction of view of the sky, the corresponding radiance is corrected to take into account the presence of obstacles. In the latter case we introduce correction factors, which we designate $K(P, \theta, \phi)$, to permit us to consider the atmosphere between point P (where the diffuse irradiance is calculated) and the obstacle in the direction (θ, ϕ) . These factors depend on the optical thickness of the atmosphere between these two points; details of their computation are given in Appendix A. The expression for the dif-

fuse irradiance that reaches point P of a rugged terrain then becomes

$$E_{\text{diffuse}}(P) = T_g^\downarrow(P, \theta_s) \left[\iint_{\Omega_{\text{sky}}(P)} L^d(z_P, \theta, \phi) \cos \theta d\omega + \iint_{\bar{\Omega}_{\text{sky}}(P)} L^d(z_P, \theta, \phi) K(P, \theta, \phi) \cos \theta d\omega \right] = T_g^\downarrow(P, \theta_s) \iint_{\Omega=2\pi} L^d(z_P, \theta, \phi) K(P, \theta, \phi) \times \cos \theta d\omega, \quad (4)$$

where $\Omega_{\text{sky}}(P)$ and $\bar{\Omega}_{\text{sky}}(P)$ are, respectively, the solid angle of view for point P and its complement in the half-space above P. The second expression is simply a condensed one, for which we assume that the K factors are equal to 1 if we consider an incident direction inside the solid angle of view of the sky. Note that angles θ and ϕ and solid angle $d\omega$ are expressed in the local system of reference of point P on the surface.

The Earth–atmosphere coupling irradiance is the most difficult term to model, as it results from complex processes in the system. In the case of flat ground, Tanré *et al.*¹⁰ suggest analytical solutions for this term. In the case of a scene that is rugged, strongly heterogeneous, or both, their approach is no longer valid. The complexity of the problem prompted us to use a Monte Carlo code⁸ in an attempt to understand the phenomenon. As a result of our analysis, we conclude that no analytical, empirical, or tabulated functions allow us to compute this component robustly for various ground and atmospheric conditions. For this reason, we decided to use a statistical Monte Carlo module to compute the Earth–atmosphere coupling irradiance.

The principle of the Monte Carlo model consists of launching photons from each point M of G, with respect to the point's received irradiance and bidirectional reflectance: Suppose that a surface dS_M about point M receives irradiance $E_{\text{direct}}(M) + E_{\text{diffuse}}(M)$, and suppose that this irradiance corresponds to N photons; some of these N photons are reflected according to the bidirectional reflectance of the surface on M, and some of these reflected photons might reach the surface dS_P near P. The Monte Carlo module permits us to compute the part $dn_{\text{coupling}}(M, P)$ of the photons that are reflected by M and that reach dS_P . The Earth–Atmosphere coupling irradiance is then given by

$$E_{\text{coupling}}(P) = \iint_G \frac{[E_{\text{direct}}(M) + E_{\text{diffuse}}(M)]}{N} \times \frac{dn_{\text{coupling}}(M, P)}{dS_P} dS_M. \quad (5)$$

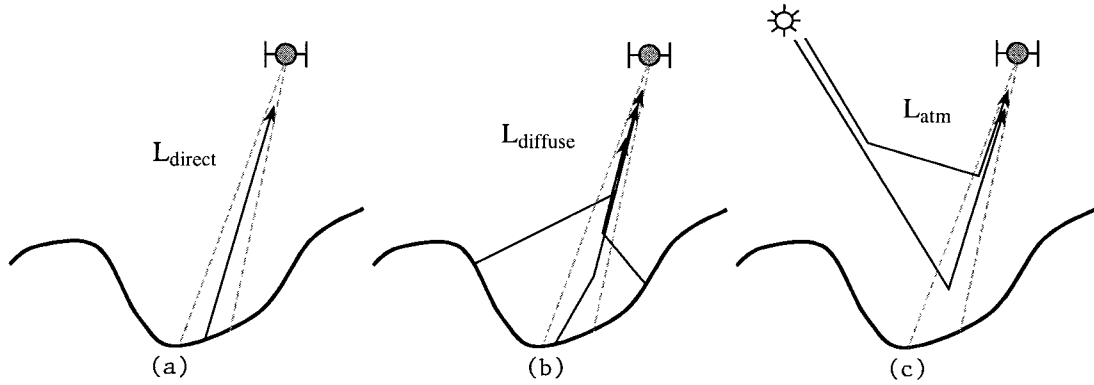


Fig. 3. Radiance components at sensor level.

This equation can be interpreted as follows: The term $[E_{\text{direct}}(M) + E_{\text{diffuse}}(M)]dS_M/N$ corresponds to the spectral energy (in watts per micrometer) that is associated with each photon launched from M, whereas $dn_{\text{coupling}}(M, P)/dS_P$ is the number of photons per surface unit reflected by surface dS_M and reaching dS_P . As we mentioned above, the global Monte Carlo method demands significant computer time, but restricting its use to this specific case has an acceptable effect on the total time consumed.

The adjacency components originate from reflections of direct and diffuse irradiance from the neighborhood. For most cases, considering only the first reflection produces satisfactory results and allows us to minimize the computation time. The contribution of an elementary surface dS_M at point M to the irradiance at P depends on several parameters: the view factor of dS_M , the bidirectional reflectance of M, and the atmospheric attenuation between M and P. Considering in a first step the direct downward irradiance and a neighborhood $V(P)$ of P, the contribution to the adjacency component is

$$E_{\text{direct-reflected}}(P) = \iint_{V(P)} E_{\text{direct}}(M) \frac{\rho_M[\hat{N}(M), \hat{n}_s, \hat{n}_{MP}]}{\pi} \times \exp[-\tau(M, P)] T_g(M, P) V_{MP} \times \frac{\langle \hat{N}(M) \cdot \hat{n}_{MP} \rangle \langle \hat{N}(P) \cdot \hat{n}_{PM} \rangle}{r_{MP}^2} dS_M, \quad (6)$$

where \hat{n}_{MP} is a unit vector oriented from M to P; $\rho_M[\hat{N}(M), \hat{n}_s, \hat{n}_{MP}]$ is the reflectance value that is related to the local slope of M, to the incident direction given by \hat{n}_s , and to the reflection direction given by \hat{n}_{MP} ; $\tau(M, P)$ and $T_g(M, P)$ are, respectively, the optical thickness and the gaseous transmission of the path between M and P; V_{MP} is a binary value set to zero if M is not visible by P; and, finally, r_{MP} is the distance between M and P. The contribution associated with the diffuse downward component has a similar expression, the only difference being in the reflectance value that has to be considered. Because of the diffuse downward component the incidence of

the signal on M is diffuse, whereas the reflection direction is well defined; we characterize the reflectance by the hemispherical directional reflectance (or plane albedo) $a_M[\hat{N}(M), \hat{n}_{MP}]$ of point M. The expression for the reflected diffuse components is thus

$$E_{\text{diffuse-reflected}}(P) = \iint_{V(P)} E_{\text{diffuse}}(M) \frac{a_M[\hat{N}(M), \hat{n}_{MP}]}{\pi} \times \exp[-\tau(M, P)] T_g(M, P) V_{MP} \times \frac{\langle \hat{N}(M) \cdot \hat{n}_{MP} \rangle \langle \hat{N}(P) \cdot \hat{n}_{PM} \rangle}{r_{MP}^2} dS_M. \quad (7)$$

To compute these adjacency components, it is necessary to define the size of the relevant neighborhood $V(P)$. However, it is difficult to have well-defined rules for determining the appropriate size because that size depends highly on the topography, the ground reflectances, and the optical thickness of the atmosphere. In most cases, a neighborhood radius of a few kilometers is sufficient, but, if slopes and reflectance values are important, that radius must be larger.

B. Radiance at Sensor Level

In the Earth-to-sensor path, most of the photons come directly from the target [Fig. 3(a)]. However, photons at the sensor level can also correspond to scattered photons coming either from the target or from neighboring ground-surface pixels [Fig. 3(b)]. Finally, photons can reach the sensor that were scattered in the atmosphere without reaching the surface [Fig. 3(c)]. They correspond to the atmospheric intrinsic radiance. The total signal received by the sensor is then obviously equal to the sum of the various signals just described:

$$L_{\text{total}} = L_{\text{direct}} + L_{\text{diffuse}} + L_{\text{atm}}. \quad (8)$$

1. Direct Upward Path

Each pixel of the sensor image is defined by the sensor position, the viewing direction, and the resolution at ground level. These properties completely define

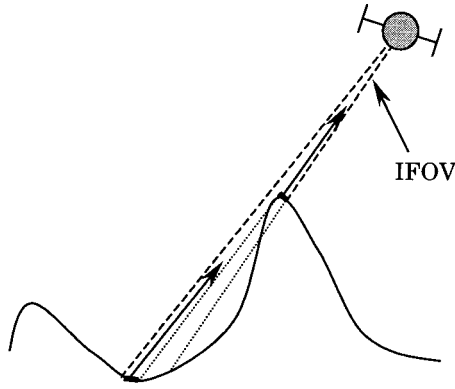


Fig. 4. Ground surface intercepted by the IFOV.

the instantaneous field of view (IFOV) of the sensor. The upward direct radiance that reaches a pixel i of the sensor is related to the ground surfaces intercepted by the IFOV of i and to the radiance reflected by these surfaces toward the sensor. Note that these intercepted surfaces do not necessarily constitute a homogeneous area, as Fig. 4 shows. Thus, to account for the eventual subpixel variability, direct upward radiance results from the average of subpixel radiances: If $L_{\text{ground}}[P, \hat{n}_v(P)]$ is the radiance reflected by a given point P at ground level toward the

sociated with the direct upward path such that the direct upward radiance is given by

$$L_{\text{direct}} = L_{\text{direct-direct}} + L_{\text{diffuse-direct}} + L_{\text{coupling-direct}} + L_{\text{direct-reflected-direct}} + L_{\text{diffuse-reflected-direct}} \quad (10)$$

Each of these terms then needs to be made explicit.

The most obvious direct radiance component results from direct downward and upward paths:

$$L_{\text{direct-direct}}(i) = \frac{1}{\Omega_i} \iint_{\Omega_i} E_{\text{direct}}(P_{d\omega}) \frac{\rho[\hat{N}(P_{d\omega}), \hat{n}_s, \hat{n}_v(P_{d\omega})]}{\pi} \times \exp[-\tau^\uparrow(P_{d\omega})/\mu_v(P_{d\omega})] \times T_g^\uparrow[P_{d\omega}, \theta_v(P_{d\omega})] d\omega, \quad (11)$$

where $\hat{n}_v(P)$ is the unit vector that gives the direction of the sensor viewed from P .

The next component comes from the diffuse irradiance reflected by the ground. Its computation is of course similar to that of its equivalent for the downward path, but the reflectance factor involved is different because the distribution of the incident energy on the ground changes. In fact, we have to compute the mean value of the reflectance involved here $\{\bar{\rho}_{\text{diffuse-direct}}[P, \hat{n}_v(P)]\}$, and, because the diffuse sky radiances are known, this value can be accurately evaluated for each ground point:

$$\bar{\rho}_{\text{diffuse-direct}}[P, \hat{n}_v(P)] = \frac{\iint_{\Omega=2\pi} L^d(z_P, \theta, \phi) K(P, \theta, \phi) \rho_P[\hat{N}(P), \hat{n}(\theta, \phi), \hat{n}_v(P)] \cos \theta d\omega}{\iint_{\Omega=2\pi} L^d(z_P, \theta, \phi) K(P, \theta, \phi) \cos \theta d\omega} \quad (12)$$

sensor, the radiance received directly by pixel i at the sensor level is

$$L_{\text{direct}}(i) = \frac{1}{\Omega_i} \iint_{\Omega_i} L_{\text{ground}}[P_{d\omega}, \hat{n}_v(P_{d\omega})] \times \exp[-\tau^\uparrow(P_{d\omega})/\mu_v(P_{d\omega})] T_g^\uparrow[P_{d\omega}, \theta_v(P_{d\omega})] d\omega, \quad (9)$$

where Ω_i is the solid angle (i.e., the IFOV) associated with pixel i ; $P_{d\omega}$ gives the position of the ground surface intercepted by elementary solid angle $d\omega$; $\tau^\uparrow(P)$ is the optical thickness of the atmosphere from point P to sensor level; $\mu_v(P) = \cos[\theta_v(P)]$ and $\theta_v(P)$ is the zenith angle of the direction defined by P and the sensor; and finally, $T_g^\uparrow[P_{d\omega}, \theta_v(P_{d\omega})]$ is the gaseous transmission from P to the sensor. $L_{\text{ground}}[P, \hat{n}_v(P)]$ may be split into several components that correspond to the various irradiance sources described in Subsection 2.A (Fig. 1). We distinguish, thus, five radiance terms as-

This reflectance can be computed simultaneously with the downward diffuse irradiance that reaches ground point P . The corresponding radiance component that reaches the sensor is then

$$L_{\text{diffuse-direct}}(i) = \frac{1}{\Omega_i} \iint_{\Omega_i} E_{\text{diffuse}}(P_{d\omega}) \times \frac{\bar{\rho}_{\text{diffuse-direct}}[P_{d\omega}, \hat{n}_v(P_{d\omega})]}{\pi} \times \exp[-\tau^\uparrow(P_{d\omega})/\mu_v(P_{d\omega})] \times T_g^\uparrow[P_{d\omega}, \theta_v(P_{d\omega})] d\omega. \quad (13)$$

The Earth-atmosphere coupling irradiance also results from diffuse incident energy, but its spatial distribution is unknown. The reflection on P is then characterized by the hemispherical directional reflectance

tance, which corresponds to the plane spectral albedo α_P and yields

$$L_{\text{coupling-direct}}(i) = \frac{1}{\Omega_i} \iint_{\Omega_i} E_{\text{coupling}}(P_{d\omega}) \times \frac{\alpha_{P_{d\omega}}[\hat{N}(P_{d\omega}), \hat{n}_v(P_{d\omega})]}{\pi} \times \exp[-\tau^\uparrow(P_{d\omega})/\mu_v(P_{d\omega})] \times T_g^\uparrow[P_{d\omega}, \theta_v(P_{d\omega})]d\omega. \quad (14)$$

Finally, we have to consider the adjacency components that come from reflections from the neighborhood. The corresponding signals result from two reflection components on the ground (one on a neighboring area and another on the target). To use the most accurate reflectance values involved, we do not introduce the irradiance values computed before; it is more efficient to rewrite the formulas completely. With respect to the direct-reflected-direct component, the incident and reflection directions are well known for each reflection, and thus we can compute the exact reflectance value; we then obtain

$$L_{\text{direct-reflected-direct}}(i) = \frac{1}{\Omega_i} \iint_{\Omega_i} \left\{ \iint_{V(P_{d\omega})} E_{\text{direct}}(M) \frac{\rho_M[\hat{N}(M), \hat{n}_s, \hat{n}_{MP_{d\omega}}]}{\pi} T_g(M, P_{d\omega}) \exp[-\tau(M, P_{d\omega})] \times \frac{\langle \hat{N}(M) \cdot \hat{n}_{MP_{d\omega}} \rangle \langle \hat{N}(P_{d\omega}) \cdot \hat{n}_{MP_{d\omega}} \rangle}{r_{MP_{d\omega}}^2} V_{MP_{d\omega}} \frac{\rho_{P_{d\omega}}[\hat{N}(P_{d\omega}), \hat{n}_{P_{d\omega}}, \hat{n}_v(P_{d\omega})]}{\pi} dS_M \right\} \times \exp[-\tau^\uparrow(P_{d\omega})/\mu_v(P_{d\omega})] T_g^\uparrow[P_{d\omega}, \theta_v(P_{d\omega})]d\omega. \quad (15)$$

The diffuse-reflected-direct radiance components are obviously quite similar. However, the first reflection cannot be defined exactly. As the computation of a mean reflectance value $\bar{\rho}_{\text{diffuse-MP}}(M, \hat{n}_{MP})$ {similar to $\bar{\rho}_{\text{diffuse-direct}}[P, \hat{n}_v(P)]$ } would require too much computation time, so we again introduce the spectral plane albedo α_M of M :

$$L_{\text{diffuse-reflected-direct}}(P) = \frac{1}{\Omega_i} \iint_{\Omega_i} \left[\iint_{V(P_{d\omega})} E_{\text{diffuse}}(M) \frac{\alpha_M[\hat{N}(M), \hat{n}_{MP_{d\omega}}]}{\pi} T_g(M, P_{d\omega}) \exp[-\tau(M, P_{d\omega})] \times \frac{\langle \hat{N}(M) \cdot \hat{n}_{MP_{d\omega}} \rangle \langle \hat{N}(P_{d\omega}) \cdot \hat{n}_{P_{d\omega}M} \rangle}{r_{MP_{d\omega}}^2} V_{MP_{d\omega}} \frac{\rho_{P_{d\omega}}[\hat{N}(P_{d\omega}), \hat{n}_{P_{d\omega}M}, \hat{n}_v(P_{d\omega})]}{\pi} dS_M \right] \times \exp[-\tau^\uparrow(P_{d\omega})/\mu_v(P_{d\omega})] T_g^\uparrow[P_{d\omega}, \theta_v(P_{d\omega})]d\omega. \quad (16)$$

2. Diffuse Upward Path

Here we consider the portion of the signal reflected by the ground surface and scattered by the atmosphere in the IFOV of any pixel i of the sensor. Figure 5 illustrates well that the energy associated with this

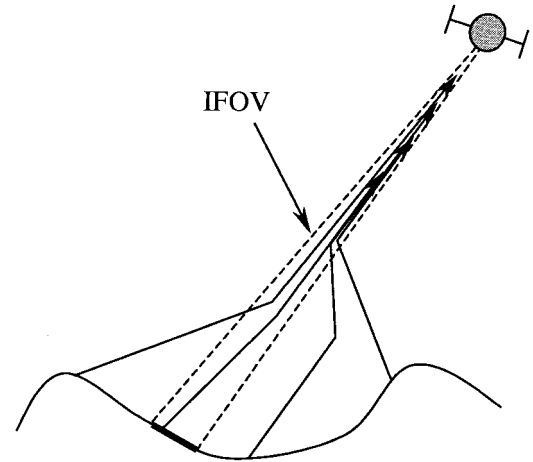


Fig. 5. Diffuse upward path.

path does not necessarily come from reflections on surfaces intercepted by the IFOV but may result from reflections from surrounding areas. The characterization of the upward diffuse path consists then of

determining a function $C_d^\uparrow(P, i)$, defined such that $C_d^\uparrow(P, i)dS_P$ indicates the proportion of signal reflected by the elementary surface dS_P about P and reaching the sensor inside the IFOV. This point-spread function has already been studied^{1,11} for flat surfaces. However, as with the Earth-atmosphere coupling term at ground level, no robust analytical or

empirical solution was found that would generally work for any topographic and atmospheric conditions. Fortunately, the computation of $C_d^\uparrow(P, i)$ can be carried out again through to a statistically specific routine that performs backward Monte Carlo¹¹ ray

tracing: As a result of the Helmholtz reciprocity principle, $C_d^\uparrow(P, i)dS_P$ is also the probability of reaching ground surface dS_P after at least one scattering by the atmosphere for a photon coming from pixel sensor i . One then uses the backward Monte Carlo method to determine this probability by launching photons from the sensor inside the IFOV of each pixel i . The photons are accounted for at ground level. Assuming that N photons are launched from pixel i of the sensor and that $dn^d(P, i)$ is the number of scattered photons that reach elementary surface dS_P near P , we can estimate $C_d^\uparrow(P, i)$ as

$$C_d^\uparrow(P, i) = \frac{1}{N} \frac{dn^d(P, i)}{dS_P}. \quad (17)$$

To compute the diffuse upward radiance that comes from the ground, one can use $C_d^\uparrow(P, i)dS_P$ as a diffuse transmission from surface dS_P to pixel sensor i . Thus the generic expression for the upward diffuse radiance reaching pixel i can be written as

$$L_{\text{diffuse}}(i) = \iint_G L_{\text{ground}}(P) C_d^\uparrow(P, i) T_g^\uparrow[P, \theta_v(P)] dS_P, \quad (18)$$

where $L_{\text{ground}}(P)$ in this case relates to the radiance reflected by the elementary surface dS_P in the entire hemisphere. Note again that the computation of $C_d^\uparrow(P, i)$ is made without gaseous absorption, whereas the corresponding transmission is introduced separately. As for the case of the direct path, we consider five different components that are associated with the diffuse path according to their downward irradiance components. As previously, the challenge at this point consists of properly introduc-

The direct-diffuse radiance component involves a known incident direction of the energy at ground level and a reflection of it in the whole hemisphere. The spectral plane albedo α_P is then introduced:

$$L_{\text{direct-diffuse}}(i) = \iint_G E_{\text{direct}}(P) \frac{\alpha_P[\hat{N}(P), \hat{n}_s]}{\pi} \times C_d^\uparrow(P, i) T_g^\uparrow[P, \theta_v(P)] dS_P. \quad (20)$$

The photons from the downward diffuse energy that reach the ground are distributed in all directions. We need then to introduce a mean reflectance value over all incident directions and all reflection directions. This value corresponds to the spherical albedo S_P . We then obtain

$$L_{\text{diffuse-diffuse}}(i) = \iint_G E_{\text{diffuse}}(P) \frac{S_P}{\pi} C_d^\uparrow(P, i) T_g^\uparrow \times [P, \theta_v(P)] dS_P. \quad (21)$$

The radiance that comes from the Earth-atmosphere coupling irradiance has similar distribution properties, so

$$L_{\text{coupling-diffuse}}(i) = \iint_G E_{\text{coupling}}(P) \frac{S_P}{\pi} C_d^\uparrow(P) T_g^\uparrow \times [P, \theta_v(P)] dS_P. \quad (22)$$

The adjacency components are again computed completely, without direct use of the corresponding irradiance terms already calculated. The reflection on the target includes a hemispherical distribution of the reflected flux; it results that

$$L_{\text{direct-reflected-diffuse}}(i) = \iint_G \left\{ \iint_{V(P)} E_{\text{direct}}(M) \frac{\rho_M[\hat{N}(M), \hat{n}_s, \hat{n}_{MP}]}{\pi} T_g(M, P) \exp[-\tau(M, P)] \times \frac{\langle \hat{N}(M) \cdot \hat{n}_{MP} \rangle \langle \hat{N}(P) \cdot \hat{n}_{PM} \rangle}{r_{MP}^2} V_{MP} \frac{\alpha_P[\hat{N}(P), \hat{n}_{PM}]}{\pi} dS_M \right\} C_d^\uparrow(P, i) T_g^\uparrow[P, \hat{n}_v(P)] dS_P, \quad (23)$$

$$L_{\text{diffuse-reflected-diffuse}}(i) = \iint_G \left\{ \iint_{V(P)} E_{\text{diffuse}}(M) \frac{\alpha_M[\hat{N}(M), \hat{n}_{MP}]}{\pi} T_g(M, P) \exp[-\tau(M, P)] \times \frac{\langle \hat{N}(M) \cdot \hat{n}_{MP} \rangle \langle \hat{N}(P) \cdot \hat{n}_{PM} \rangle}{r_{MP}^2} V_{MP} \frac{\alpha_P[\hat{N}(P), \hat{n}_{PM}]}{\pi} dS_M \right\} C_d^\uparrow(P, i) T_g^\uparrow[P, \hat{n}_v(P)] dS_P. \quad (24)$$

ing the appropriate reflectances. As for the direct upward case, the diffuse upward radiance is a sum of five contributions associated with the five ground-surface irradiance components:

$$L_{\text{diffuse}} = L_{\text{direct-diffuse}} + L_{\text{diffuse-diffuse}} + L_{\text{coupling-diffuse}} + L_{\text{direct-reflected-diffuse}} + L_{\text{diffuse-reflected-diffuse}}. \quad (19)$$

3. Atmospheric Intrinsic Radiance

Another origin of energy at the sensor level also has to be taken into account in the present model. It consists of photons that reach the sensor after having been scattered one or more times in the atmosphere, without reflections on the ground. It is termed the atmospheric intrinsic radiance, and it depends on the

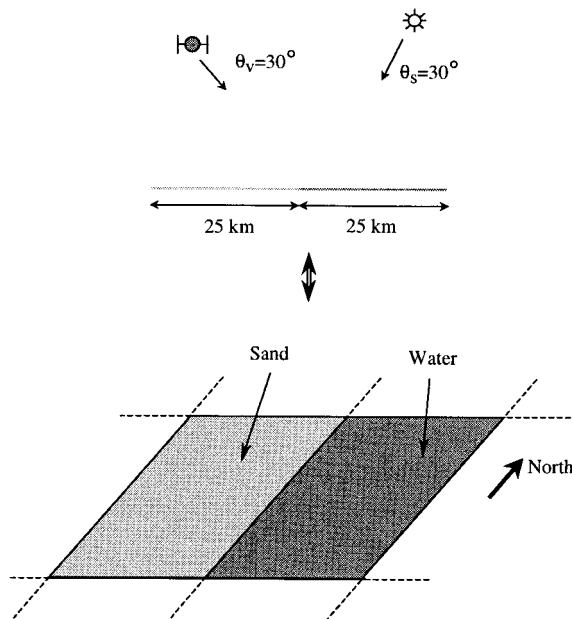


Fig. 6. Seashore landscape.

viewing angle and on the thickness of the atmosphere between the ground and the sensor, which means that altitude of the ground is a significant factor in the value of this energy (as was demonstrated by Dozier and Frew¹²). Because of the spatial low-pass effects of the atmosphere, the ground variations are not completely transmitted in the atmospheric radiance; we choose, however, to follow the computation

method suggested by Richter,⁷ which consists in taking into account the altitude of the viewed area at ground level. With this assumption, all parameters (solar and viewing conditions, ground target, and sensor altitudes) are known; one then uses the 6S code to compute the corresponding atmospheric radiance (L_{atm}).

3. Comparison of the Radiative Transfer Code with a Reference Code

In this section we check the validity of the AMARTIS model described in Section 2. The AMARTIS model has been compared with the 6S code over flat and homogeneous ground surfaces for various atmospheric and observing conditions. Because our model uses similar assumptions for such configurations, the comparisons show differences of less than 1%. However, the 6S code is not able to deal with topographic and complex environmental effects, so it is essential to validate the AMARTIS model more thoroughly. To this end, a Monte Carlo radiative transfer code⁸ is used and taken as a reference code. The comparison of a set of results from both codes in various atmospheric and ground configurations permits the evaluation of the physical model developed here and the assumptions made. The first configuration that we evaluate consists of flat ground that has a linear boundary between two soil types. The main analysis then concerns the environmental effects produced by this reflectance gap. In two additional cases we introduce significant topological relief, because modeling topographic effects is the

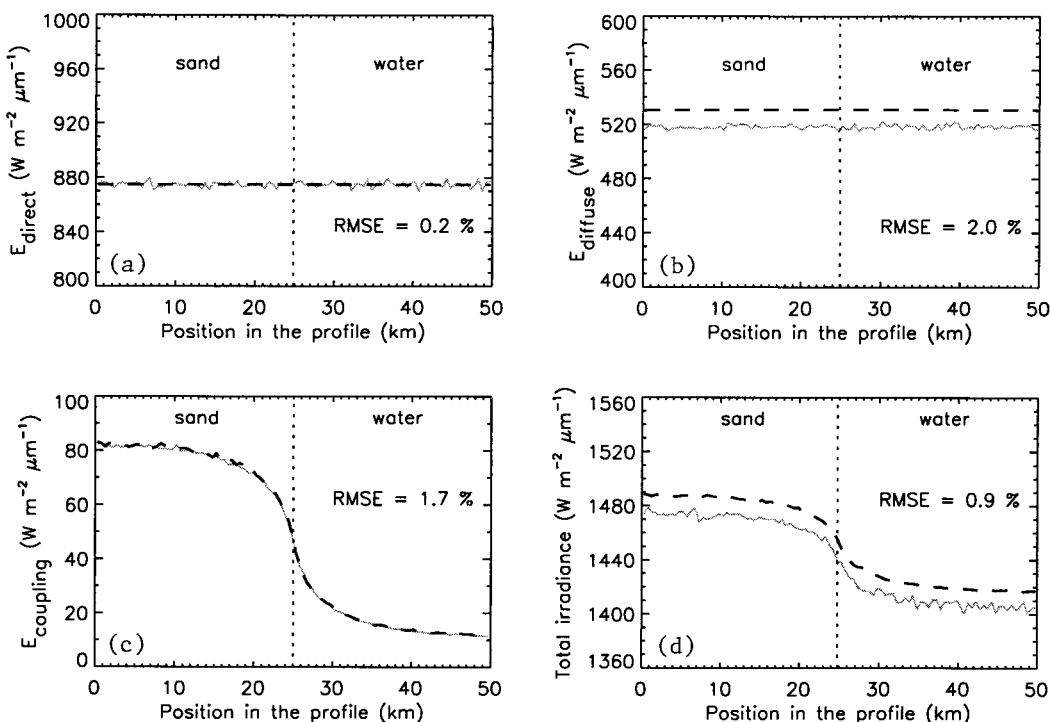


Fig. 7. Irradiance components at ground level on the seashore. In this and the figures below, the solid, lighter curves represent the Monte Carlo model and the dashed, darker curves represent the physical model. RMSE, root-mean-square error.

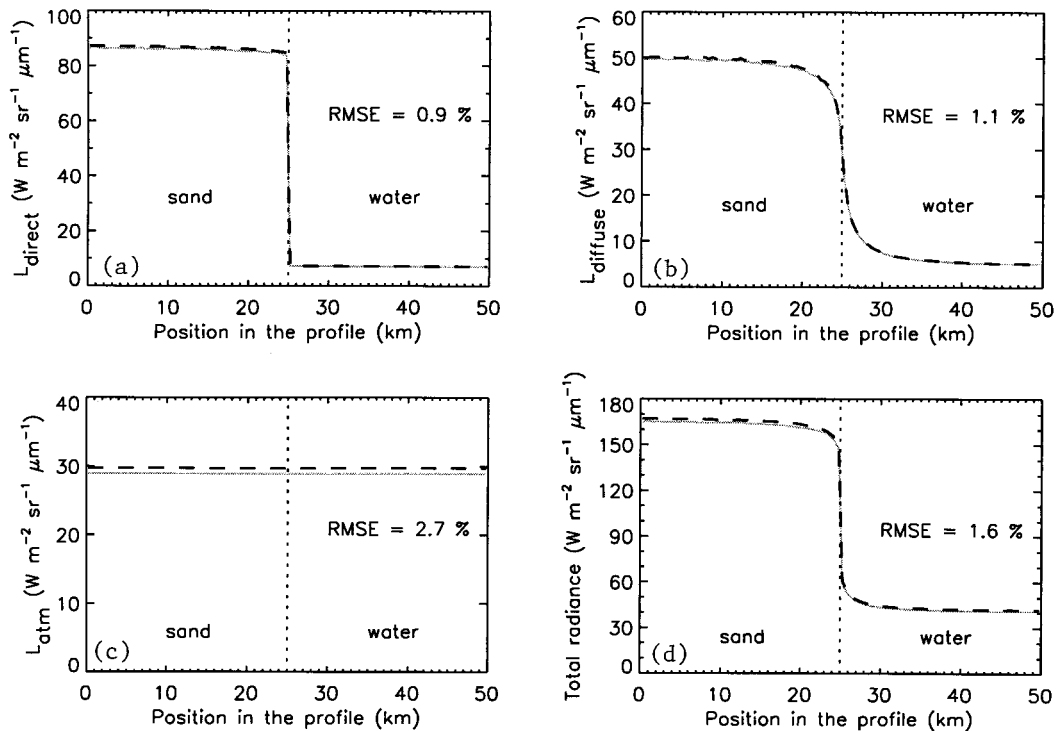


Fig. 8. Radiance components received by the sensor over the seashore.

chief feature of the code that we wish to evaluate. The second configuration corresponds to a desert landscape composed of linear dunes, whereas third configuration is an extreme case in which highly reflecting surfaces on very steep slopes present a severe test of the portions of the model that are influenced by topographic effects.

In the following discussion we focus mainly on the differences observed in the results of the two codes for each modeled component, because a detailed analysis of the total signal has already been made for these configurations.⁸ Moreover, all the scenes considered in this section are described by a profile that is invariant along an axis orthogonal to this profile. As a result, any component is completely known when it is described over the landscape profile. For this reason, the plots of the irradiance components will be made in terms of the components' positions in the profile. Because sensor IFOV's are characterized by the sensor's position and a horizontal grid at ground level that corresponds to the sensor's spatial resolution, the radiance components also are plotted this way.

A. Reflectance Step at Ground Level

In the first case that we consider, the ground surface is flat. We consider here a wide seashore, which means two types of surface (sand and seawater), which produce a linear boundary (Fig. 6). At a wavelength of 550 nm the reflectances are assumed to be Lambertian and their values are 0.35 for sand and 0.03 for water.¹³ We used a standard mid-latitude winter atmospheric model¹⁴ with an aerosol

loading distribution that follows the Junge power law and a visibility of 10 km. The solar zenith is arbitrarily fixed at a zenith of 30°, and the Sun has an incidence azimuth angle of 90°. The satelliteborne sensor (at an altitude of 800 km) views the scene with a zenith angle also of 30° and is located on the principal (solar) plane, opposite the Sun. These geometric characteristics are illustrated in Fig. 6.

The irradiance components calculated by both the

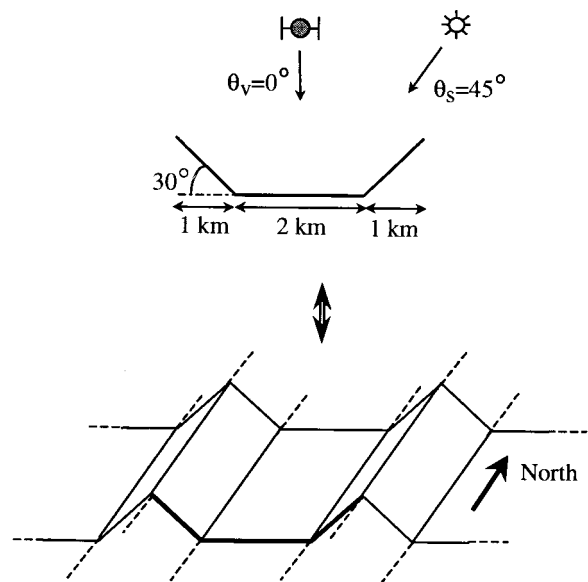


Fig. 9. Linear sand dunes.

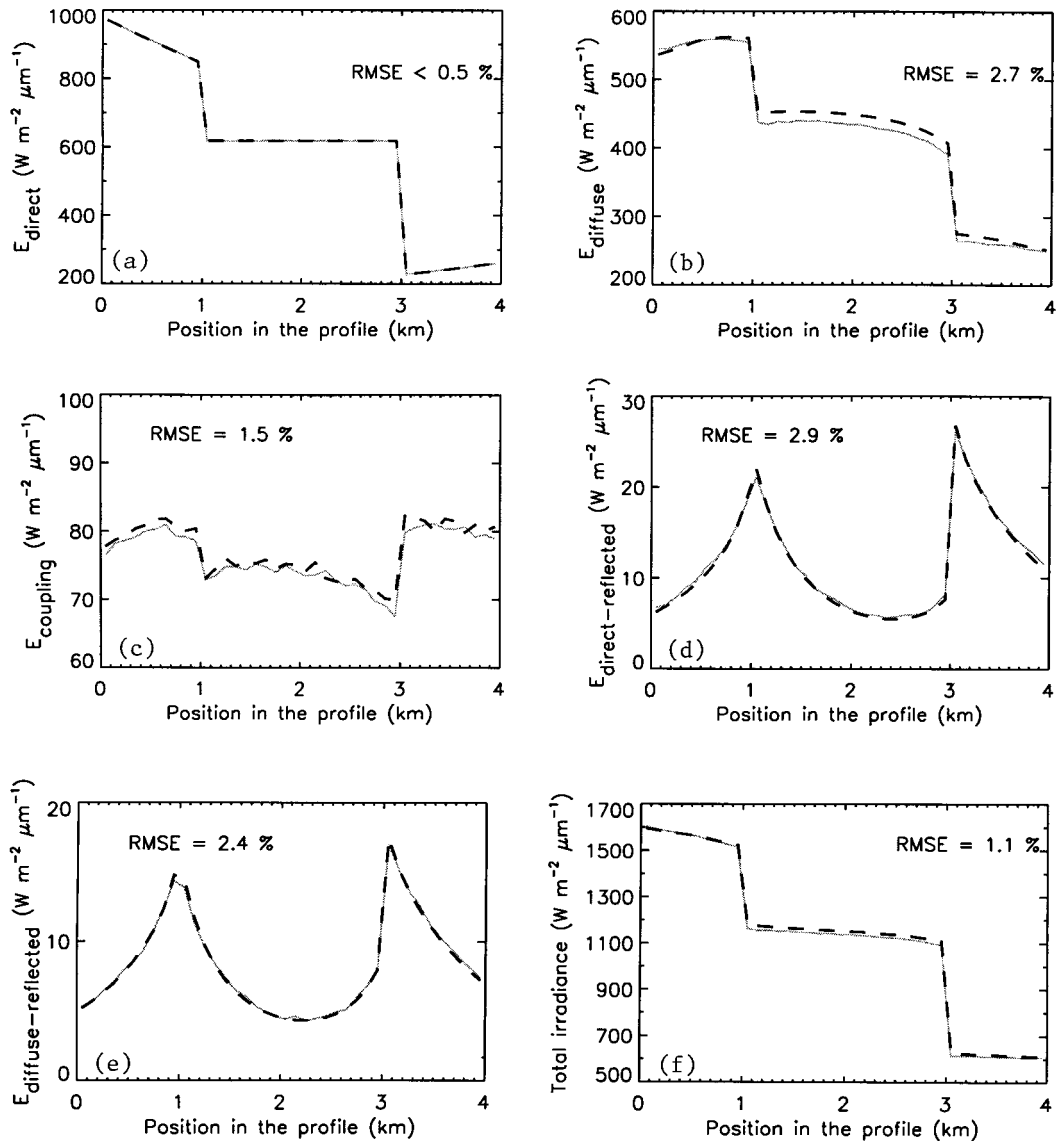


Fig. 10. Irradiance terms over linear sand dunes.

Monte Carlo code and the physical model are plotted in Fig. 7. The direct irradiance [Fig. 7(a)] is the easiest to model, and the corresponding computed values show no difference, as expected. The Monte Carlo method was run until the total signals (i.e., at ground and satellite levels) reach a convergence of better than 0.5%, which explains the noisy aspect of the Monte Carlo curves. The diffuse irradiance [Fig. 7(b)] over the flat scene is the key component in this comparison, as it involves two different methods of computing the sky diffuse radiances. The physical model used in the AMARTIS model (and based on a successive order resolution method) overestimates the Monte Carlo method by $\sim 2\%$. This error cannot be traced to the uncoupling of the gaseous absorption because there is a same-sized bias that uses a nonabsorbing atmospheric model. Rather, the bias comes from the resolution methods themselves (mainly from digitization of space and

rounding of numbers in the iterative method). It reaches reasonable values here, however, because the atmospheric optical depth (0.5) here is important.

The Earth-atmosphere coupling term [Fig. 7(c)], unlike the other terms, is not invariant over the profile because it is related to the spatial variability of the environmental reflectances. The decrease of this component from 0 to 50 km results from the progressive decrease of the mean reflectance value of the environment. The Earth-atmosphere coupling effects are modeled identically in both codes, i.e., by the same statistical method. For the physical model, the starting conditions are given by the direct and diffuse irradiances [See Eq. (4)]. Consequently, the difference calculated over the profile for the environmental component (1.7%) is due to the error in the diffuse irradiance and convergence noise. Finally, the total irradiance at ground level [Fig. 7(d)]

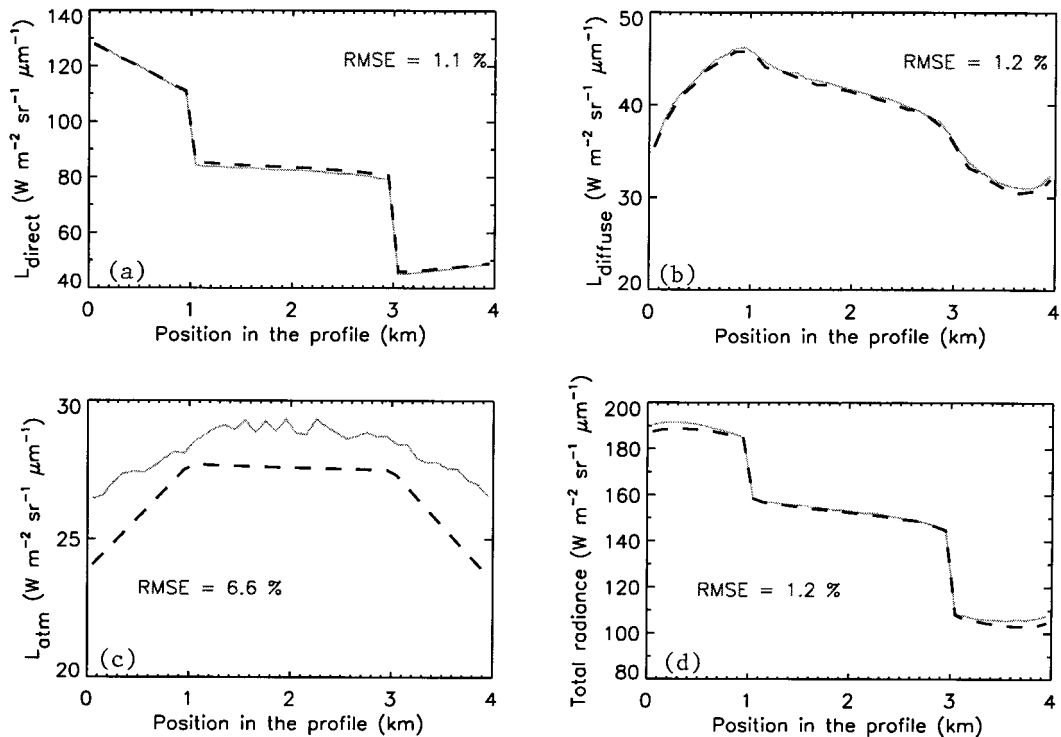


Fig. 11. Radiance terms observed over linear sand dunes.

shows good agreement between AMARTIS and Monte Carlo codes: The bias is less than 1%.

The radiance components at sensor level are plotted similarly in Fig. 8. The direct upward path is again the easiest to compute, so the associated radiance [Fig. 8(a)] is subject to the propagation of the error of the total signal only at ground level, i.e., to less than a 1% difference. The upward diffuse path is characterized without gaseous absorption owing to the backward statistical simulation used in the physical model. The gaseous transmission is considered separately, but, similarly to the case of the downward diffuse path, it does not appear to produce significant error. Consequently, the upward diffuse radiance [Fig. 8(b)] does not introduce more divergence than that observed at ground level (i.e., ~1%). The main source of error in the AMARTIS code is the atmospheric intrinsic radiance [Fig. 8(c)]. The gaseous absorption uncoupling, as before, is not responsible for the error; rather, the error comes from the computation method (based on the 6S code in the physical model), which uses tabulated values to trade off accuracy for speed of execution. However, even for the thick atmosphere considered here (the total optical thickness is greater than 0.5) and for low reflecting ground surfaces (such as water), the AMARTIS and the Monte Carlo models differ by less than 2%. Over sand (higher reflectance), the difference reduced to almost 1%.

B. Topographic Effects over Linear Dunes

This second validation step deals with a desert landscape composed of linear sand dunes, such as those

found in the Sahara (Fig. 9).¹⁵ Its topography is illustrated in Fig. 9. The linear dunes are entirely covered by sand and have a Lambertian reflectance of 0.4 at 550 nm. The atmospheric model is again the mid-latitude winter profile¹⁴ with a 10-km aerosol visibility. The Sun's zenith angle is set to 45°, and the principal plane is orthogonal to the direction of the dunes. This configuration gives low illumination on one side of the dune, as a result of the low local incidence of the solar beam.

Figure 10 shows the irradiance components at ground level. The direct irradiance [Fig. 10(a)] illustrates the effect of slope on the incident beam. Because this effect is simple to account for, the results are quite good. The previous simulation showed a bias of ~2% for the diffuse irradiance. This bias was attributed to the iterative Gauss-Seidel computation method. Over the rugged surface, the diffuse irradiance [Fig. 10(b)] has a bias that reaches 2% over the well-exposed area (on the left side of the profile) and almost 3% on the central and right sides of the profile. In spite of the disturbance of the topography and the uncoupling of the gaseous absorption, the corrections performed for the diffuse sky radiances and the integration method appear to be satisfactory. As previously, the Earth-atmosphere coupling component [Fig. 10(c)] is noisy, because it is the most demanding in terms of convergence. However, the difference does not exceed 1.5% globally. The adjacency components come from reflections in the neighborhood. They reach their maxima near both corners of the profile (at the bottom of the dunes) because the viewing angle of the neighborhood is the greatest there.

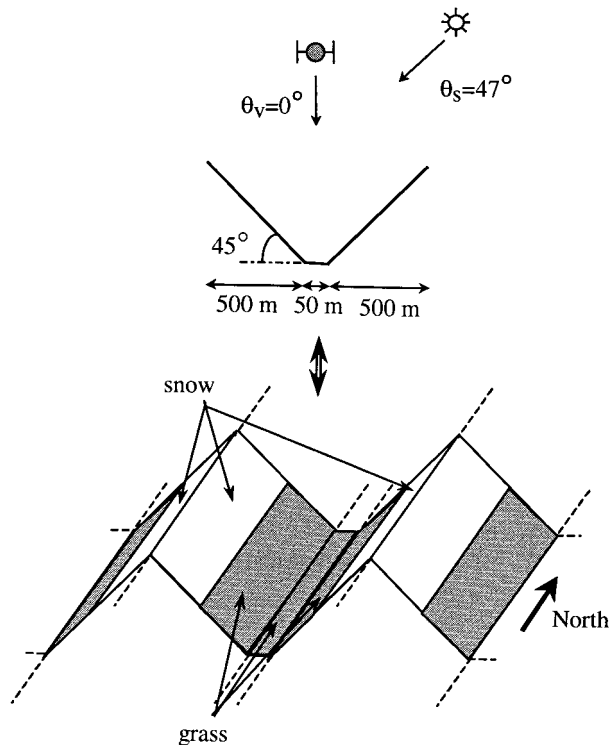


Fig. 12. Deep valley between snow-covered hilltops.

Both Earth-atmosphere coupling and adjacency effects contribute significantly to the total signal received at ground level, especially for the poorly exposed area. They thus need to be properly evaluated. Figures 10(d) and 10(e) demonstrate that the size of the neighborhood (here the radius is set to 5 km) and the single reflection alone produce consistent results (the RMSE is less than 3%). Thus, at ground level, we obtain a global error of 1.1% [Fig. 10(f)].

As in the previous simulation, the direct and diffuse upward radiances [Figs. 11(a) 11(b)] simply propagate the ground-surface bias, because the characterization of the corresponding paths introduces a few assumptions. With respect to the atmospheric intrinsic radiance, we introduce in the AMARTIS model a dependence on the altitude of the ground surface intercepted by the IFOV that at first may seem to be too important because of the low-pass effect of the atmosphere (especially for a satellite-borne sensor that views through the entire atmosphere and is at an altitude hundreds of times greater than the altitude of the highest topographic feature). Nevertheless, the altitude dependence introduces an error that is maximum in the case of satellite acquisitions over areas of highest altitude (which fortunately are few), as Fig. 11(c) illustrates. However, the global bias for this atmospheric component ($\sim 7\%$) is due mainly to the computation method (based on the speed-optimized 6S code); the altitude-dependent assumption is then appropriate. On the total signal received by the sensor [Fig. 11(d)], the estimation of the atmospheric intrinsic radiance generates a bias of 2% over the poorly exposed area on the right-hand

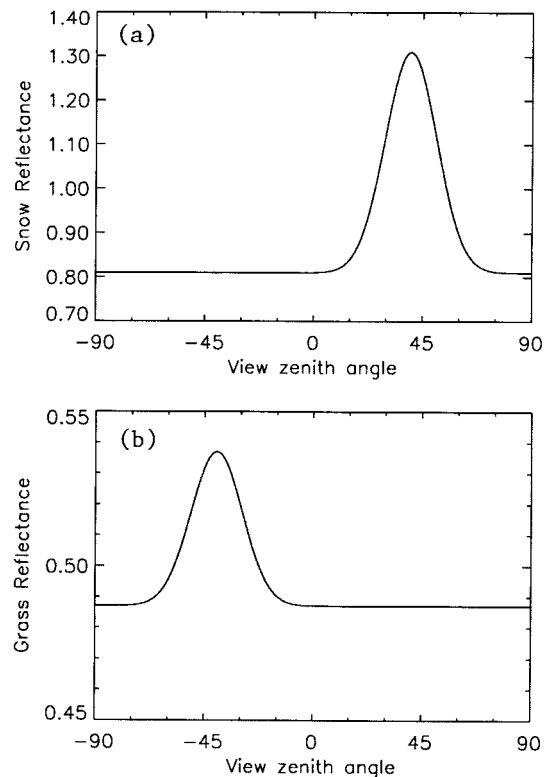


Fig. 13. Reflectance models of snow and grass. Negative zenith values are used for backward scattering.

side of the profile and of less than 1.5% over the rest of the scene.

C. Shadow Effect on Highly Reflecting Ground

Finally, to assess the robustness of the AMARTIS method in modeling topographic effects, we consider an extreme configuration that introduces severely constraining conditions. The scene is a deep valley of short green grass between snow-covered hills (Fig. 12). Owing to a lack of available data for high zenith angles, we use simple reflectance models that roughly reproduce the bidirectional reflectance behavior of snow and short grass. These models consist of a diffuse (Lambertian) term added to a Gaussian term for forward scattering (of snow) or backward scattering (of vegetation). The spectral albedos at 850 nm of each surface type (0.85 for snow and 0.49 for grass) are chosen from the ASTER database.¹³ The reflectance values of the models in the principal plane for an incidence of 40° are illustrated in Fig. 13. The atmospheric model is kept unchanged, and the aerosol visibility is set to 23 km. To create a shadowed area, we increase the solar zenith angle to 47° , and place the sensor at satellite level and configure the sensor for nadir viewing.

The comments made above for the direct and diffuse irradiance components [Figs. 14(a) and 14(b)] also apply in this case. Even over the shaded area of the terrain, the computation of these quantities produces similar biases, i.e., a negligible error for the direct path and a difference of 2% for the diffuse path.

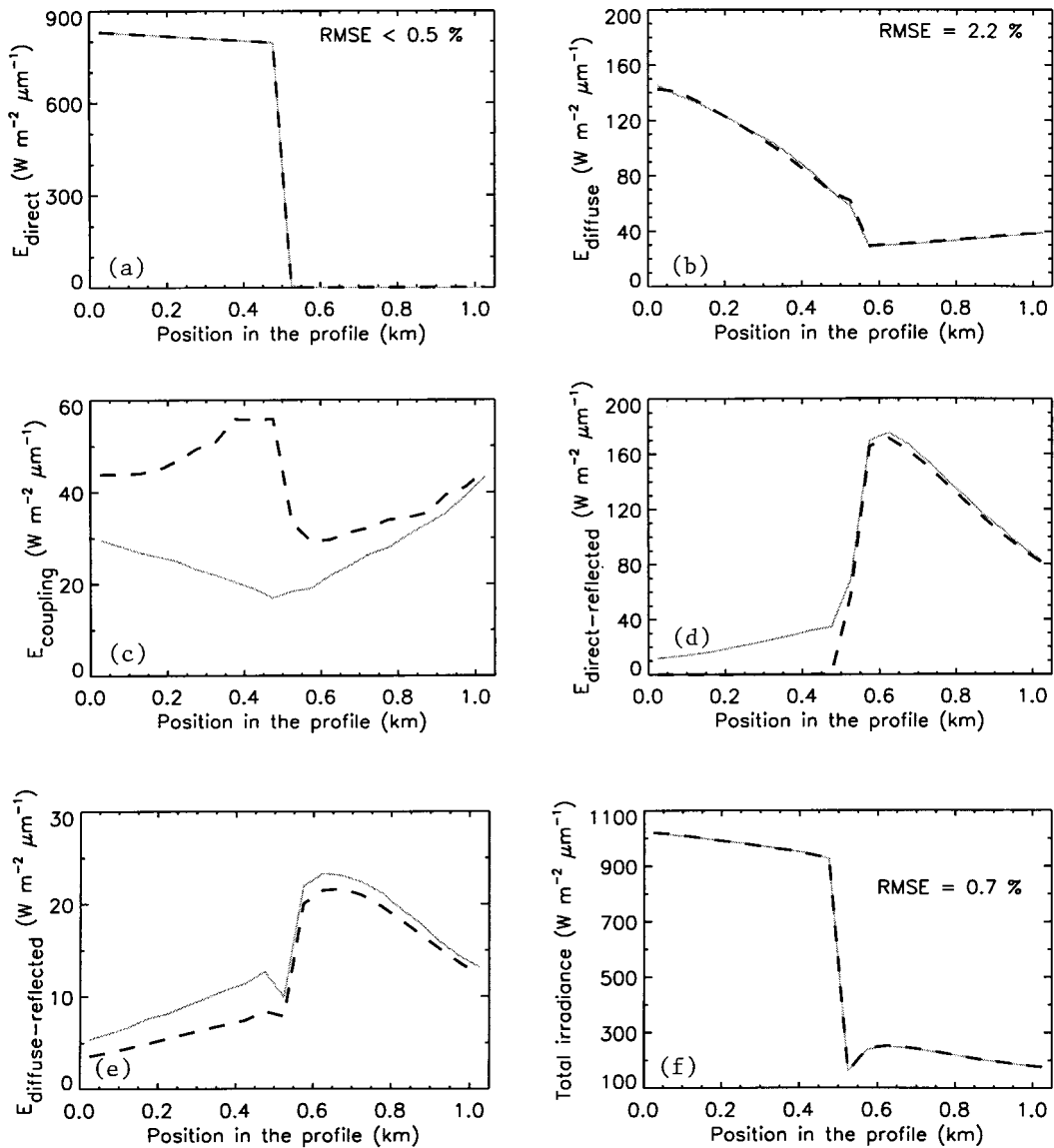


Fig. 14. Irradiance terms over the deep valley.

The plot of the Earth–atmosphere coupling term may *a priori* be surprising. In fact, there is a slight difference in the attribution of photons to the different components in the two computation methods. In the AMARTIS model the adjacency components [Figs. 14(d) and 14(e)] treat the first reflection only, which normally is sufficient (as was shown in Subsection 3.B). However, the eventual second reflections are attributed to the Earth–atmosphere coupling term [Fig. 14(c)] because it is easy to count the corresponding photons in the Monte Carlo routine. In the Monte Carlo code, the photons that are reflected several times on ground surface without scattering between them are associated with the adjacency components. For these reasons, in this validation test the environment and adjacency components have to be compared, as shown in Fig. 15. The figure shows good consistency in the results; the error is less than 1.5%. Note that for this configuration of highly

reflecting ground and clear atmosphere the radius of the neighborhood has been increased to 10 km. As a result, the values of the signal at ground level [Fig. 14(f)] computed by the two methods are almost identical. The bias is less than 1%, even in the shaded area.

The characterization of the upward direct and diffuse paths takes advantage of the moderating effects of the atmosphere. Thus the biases observed are less than 1% [Figs. 16(a) and 16(b)]. The atmospheric intrinsic radiance is low because the atmosphere is clear. The computation of this component is subject to important relative errors [Fig. 16(c)], again mostly as a result of the computation routine. Finally, the total signal received by the satelliteborne sensor [Fig. 16(d)] does not show significant errors: the bias reaches ~2% over the shaded area and is obviously less over the well-exposed part of the profile.

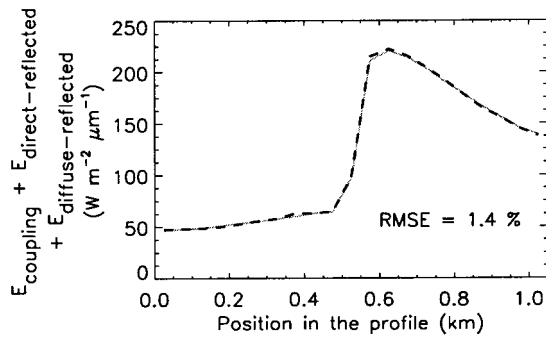


Fig. 15. Environment and adjacency irradiance over the deep valley.

In summary, the physical model AMARTIS gives satisfactory results, even for extreme conditions. It can be considered well adapted to providing accurate estimations of the radiative signal received by a given sensor that views rugged and heterogeneous scenes.

4. Conclusion

In this study a radiative transfer model for the solar reflective spectral domain has been developed that is valid over rugged and heterogeneous ground surfaces. The objective of the study was to develop a code that would provide an accuracy comparable with that of Monte Carlo methods for such conditions that would be not nearly so computationally demanding. To this end, we improved an existing and fast-resolution-type algorithm to take into account both topography and spatial variability. The resolution

method consists in identifying first the irradiance components at ground level and then the radiance components that reach the sensor. Physical modeling of each component is carried out in a second step. To allow or to optimize computation of the various fluxes at ground and sensor levels, we introduced simplifying assumptions in the modeling. The effects of these assumptions on model accuracy were checked for various observing conditions by use of a Monte Carlo resolution-method code taken as the reference. A comparison of the AMARTIS and other codes shows that they are in close agreement, even for the most complex terms related to scattering and environmental effects. The most important difference comes from the evaluation of atmospheric intrinsic radiance, which is calculated in our model with the 6S code. Nevertheless, the total number of errors is low for most of the common cases, and this demonstrates the usefulness and validity of the method presented here. Moreover, if we consider the third case presented in this paper, the proposed AMARTIS model is 100 times faster than the Monte Carlo method (a typical Unix workstation, which needs less than 10 min to run AMARTIS and more than a day to perform the Monte Carlo simulation for this case).

Our AMARTIS code is, thus, beneficial in most normal remote-sensing applications because it facilitates accurate evaluation of the radiance that reaches an airborne or a satelliteborne sensor for visible and near-infrared wavelengths with reasonable computation times. For example, it is at present used for computing the upward radiance that

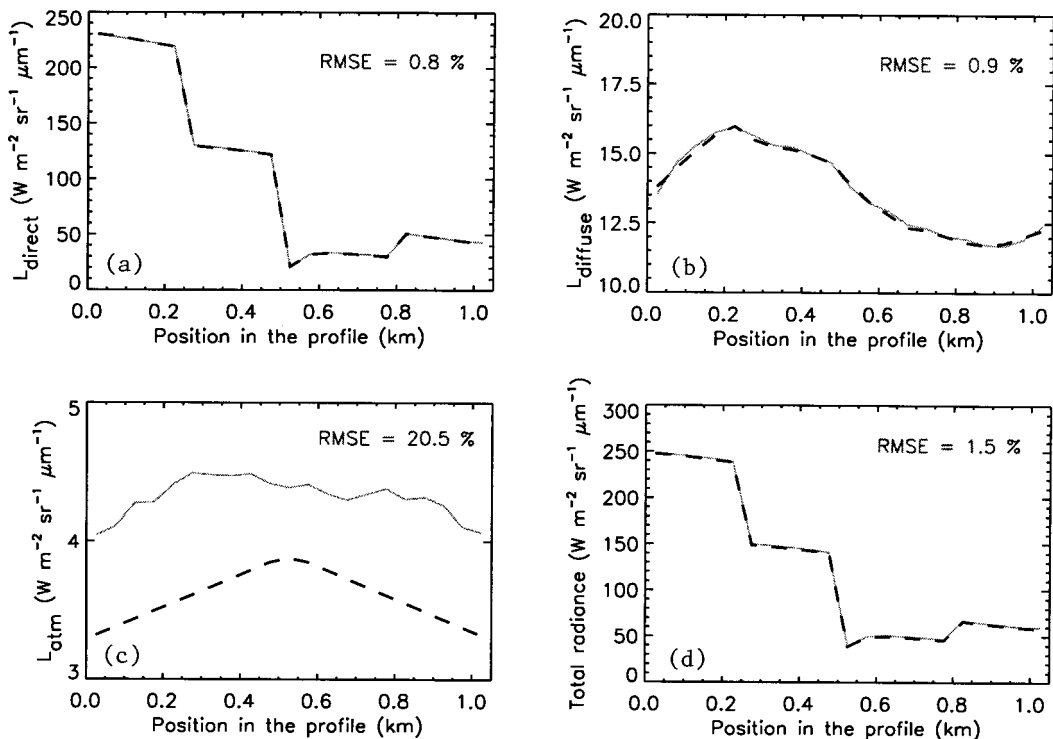


Fig. 16. Radiance components over the deep valley.

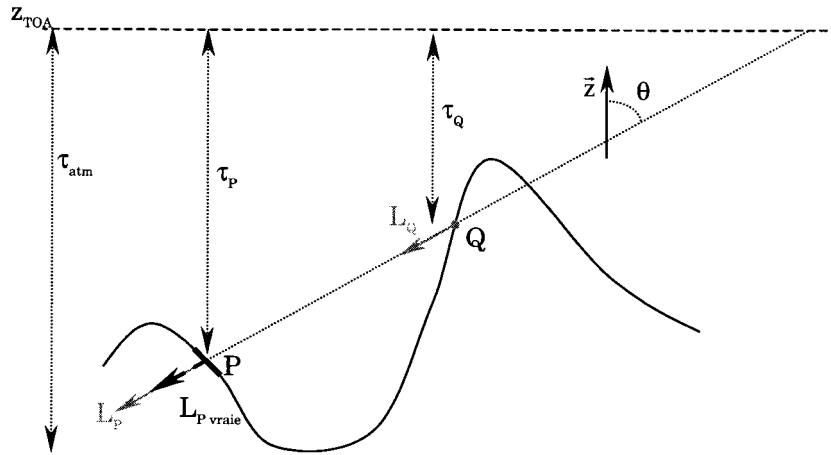


Fig. 17. Topographic effect on the sky diffuse radiances.

comes from a shaded area at ground level to establish adapted specifications for new instruments; additional ways to improve the present code are being studied. The first extension consists of taking into account the polarization of light's propagation through the Earth-atmosphere system. It is also planned to extend the model into the thermal infrared by developing a physical model that deals with the emissivity of the ground and atmospheric particles.

Appendix A

In this appendix we calculate the correction factors introduced in the diffuse irradiance formula [see Eq. (4)]. These factors are needed to correct the values of the diffuse sky radiances that are calculated for a flat ground surface, to make them applicable to a topographically variable surface. To simplify this complex problem we calculate the correction factors with the single-scattering assumption. Let us consider a ground point P and a direction (θ, ϕ) outside the sky viewing solid angle. Q is the intersection of this direction and the obstacle that hides the sky (Fig. 17). With the single-scattering assumption, one obtains the radiance observed at P in the direction (θ, ϕ) by removing the diffuse radiance L_Q , calculated for point Q with the flat-ground assumption and subsequently attenuated by the atmospheric transmission from Q to P, from the diffuse radiance L_P calculated for P also with the flat-ground assumption. In practice, the correction consists simply of removing from L_P that proportion of the radiance that comes from scattering above point Q in the direction being considered. For radiance $L_{P \text{ relief}}$ this gives

$$L_{P \text{ relief}} = L_P - L_Q \exp[-|\tau_P - \tau_Q|/\mu], \quad (\text{A1})$$

where τ_P and τ_Q are the optical thicknesses of the atmosphere above P and Q, respectively, and $\mu = \cos \theta$. The K factors can then be retrieved by evaluation of the expressions for L_P and L_Q . To this end we distinguish three different cases: downward, upward, and horizontal sky radiances.

1. Downward Sky Radiance

Let us suppose that $L_{\text{TOA}}(\theta_s, \phi_s)$ is the solar radiance at the top of atmosphere, τ_{atm} is the optical thickness of the atmosphere, and $p(\theta_1, \phi_1, \theta_2, \phi_2)$ is the global phase function of the atmosphere. As Fig. 18 illustrates, the elementary contribution of layer $d\tau$ to the downward radiance that reaches a point M can be written as

$$dL_M(\theta, \phi) = L_{\text{TOA}}(\theta_s, \phi_s) \exp(-\tau/\mu_s) \frac{p(\theta_s, \phi_s, \theta, \phi)}{4\pi} \times \exp[-(\tau_M - \tau)/\mu] \frac{d\tau}{\mu_s}, \quad (\text{A2})$$

where $\mu_s = \cos \theta_s$. If this expression is integrated from $\tau = 0$ to $\tau = \tau_M$ we obtain

$$L_M(\theta, \phi) = L_{\text{TOA}}(\theta_s, \phi_s) \exp(-\tau_M/\mu) \frac{p(\theta_s, \phi_s, \theta, \phi)}{4\pi\mu_s} \frac{\mu_s\mu}{\mu - \mu_s} \times \{1 - \exp[-\tau_M(1/\mu_s - 1/\mu)]\}. \quad (\text{A3})$$

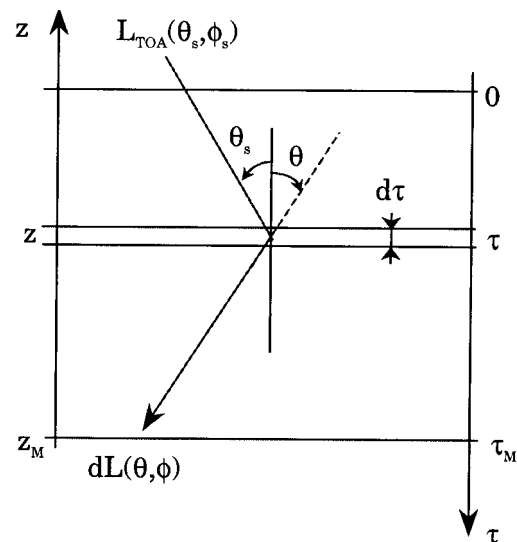


Fig. 18. Downward radiance.

Then, by replacing M successively by P and then by Q, we observe radiance that is given by

$$L_{P \text{ relief}}(\theta, \phi) = L_P - L_Q \exp[-(\tau_P - \tau_Q)/\mu] \\ = L_P \left\{ 1 - \frac{1 - \exp[-\tau_P(1/\mu_s - 1/\mu)]}{1 - \exp[-\tau_Q(1/\mu_s - 1/\mu)]} \right\}. \quad (\text{A4})$$

2. Upward Sky Radiance

For upward sky radiance as illustrated in Fig. 19, the atmosphere below point M makes a dominant contribution. Similarly to the previous case, it is required first that the elementary contribution of layer $d\tau$ to the diffuse radiance reaching M be written as

$$dL_M(\theta, \phi) = L_{\text{TOA}}(\theta_s, \phi_s) \exp(-\tau/\mu_s) \frac{p(\theta_s, \phi_s, \theta, \phi)}{4\pi} \\ \times \exp[-(\tau - \tau_M)/\mu] \frac{d\tau}{\mu_s}, \quad (\text{A5})$$

which is then integrated from τ_M to τ_{atm} :

$$L_M(\theta, \phi) = L_{\text{TOA}}(\theta_s, \phi_s) \exp(-\tau_M/\mu) \frac{p(\theta_s, \phi_s, \theta, \phi)}{4\pi\mu_s} \\ \times \frac{\mu_s\mu}{\mu_s + \mu} \{1 - \exp[-(\tau_{\text{atm}} - \tau_M)(1/\mu_s + 1/\mu)] \\ + 1/\mu\}. \quad (\text{A6})$$

Finally, similarly to the previous case, τ_M is successively replaced by τ_P and τ_Q , which results in

$$L_{P \text{ relief}}(\theta, \phi) = L_P - L_Q \exp[-(\tau_Q - \tau_P)/\mu] \\ = L_P \left\{ 1 - \frac{1 - \exp[-(\tau_{\text{atm}} - \tau_Q)(1/\mu_s + 1/\mu)]}{1 - \exp[-(\tau_{\text{atm}} - \tau_P)(1/\mu_s + 1/\mu)]} \right. \\ \left. \times \exp[-(\tau_Q - \tau_P)/\mu - (\tau_Q - \tau_P)/\mu_s] \right\}. \quad (\text{A7})$$

3. Horizontal Sky Radiance

Horizontal sky radiance is the easiest of the three kinds of radiance to deal with. Each point located along the direction under consideration is a potential source of diffuse radiance. The radiance scattered by all the points, however, is identical. So we can write

$$L_P = L(\pi/2, \phi) \int_0^\infty \exp(-\sigma_e r) dr,$$

where $L(\pi/2, \phi)$ is the radiance scattered by element dr of the horizontal path and σ_e is the total extinction coefficient of the atmosphere for the altitude consid-

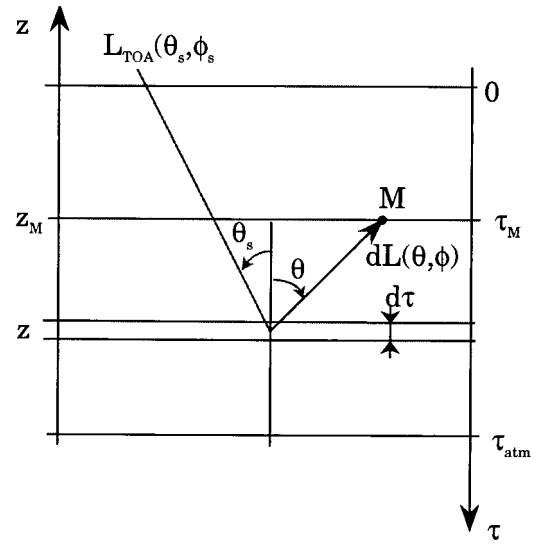


Fig. 19. Upward radiance.

ered. If there is an obstacle that hides the sky at a distance r_0 , we then have

$$L_{P \text{ relief}} = L(\pi/2, \phi) \int_0^{r_0} \exp(-\sigma_e r) dr \\ = L_P \frac{\int_0^{r_0} \exp(-\sigma_e r) dr}{\int_0^\infty \exp(-\sigma_e r) dr} \\ = L_P \{1 - \exp(-\sigma_e r_0)\}. \quad (\text{A8})$$

The expressions for the K factors are then extracted from Eqs. (A4), (A7), and (A8) when the direction considered is outside the solid angle of view of the sky:

$$K(L^\downarrow) = 1 - \frac{1 - \exp[-\tau_P(1/\mu_s - 1/\mu)]}{1 - \exp[-\tau_Q(1/\mu_s - 1/\mu)]}, \\ K(L^\uparrow) = 1 - \frac{1 - \exp[-(\tau_{\text{atm}} - \tau_Q)(1/\mu_s + 1/\mu)]}{1 - \exp[-(\tau_{\text{atm}} - \tau_P)(1/\mu_s + 1/\mu)]} \\ \times \exp[-(\tau_Q - \tau_P)/\mu - (\tau_Q - \tau_P)/\mu_s], \\ K(L^\rightarrow) = 1 - \exp(-\sigma_e r_0). \quad (\text{A9})$$

If the radiance does not require such a correction, i.e., if the direction is within direct view of the sky, the K factor is set to 1. This allows us to write the expression for the incident diffuse irradiance with a single integral [Eq. (4)].

References and Notes

1. E. Vermote, D. Tanré, J. L. Deuzé, M. Herman, and J. J. Morcrette, "Second simulation of the satellite signal in the solar spectrum, 6S: an overview," *IEEE Trans. Geosci. Remote Sens.* **35**, 675–686 (1997).

2. A. Berk, L. S. Bernstein, and D. C. Robertson, "MODTRAN: a moderate resolution model for LOWTRAN 7," NASA Tech. Rep. AD-A21433 (Spectral Sciences, Burlington, Mass., 1989).
3. B. N. Holben and C. O. Justice, "The topographic effect on spectral response from nadir-pointing sensors," *Photogramm. Eng. Remote Sens.* **46**, 1191–1200 (1980).
4. D. S. Kimes and J. A. Kirchner, "Modeling the effects of various radiant transfers in mountainous terrain on sensor response," *IEEE Trans. Geosci. Remote Sens.* **GE-19**, 100–108 (1981).
5. C. Proy, D. Tanré, and P. Y. Deschamps, "Evaluation of topographic effects on remotely sensed data," *Remote Sens. Environ.* **30**, 21–32 (1989).
6. T. Kusaka and Y. Kawata, "Atmospheric and topographic correction of satellite data over mountainous terrain," in *Proceedings of International Geoscience and Remote Sensing Symposium* (Institute of Electrical and Electronics Engineers, Piscataway, New York N.J., 1994), Vol. 1, pp. 58–60.
7. R. Richter, "Correction of atmospheric and topographic effects for high spatial resolution satellite imagery," *Int. J. Remote Sens.* **18**, 1099–1111 (1997).
8. C. Miesch, X. Briottet, Y. H. Kerr, and F. Cabot, "Monte Carlo approach for solving the radiative transfer over rugged and heterogeneous areas," *Appl. Opt.* **36**, 7419–7430 (1999).
9. B. M. Herman and S. R. Browning, "A numerical solution to the equation of radiative transfer," *J. Atmos. Sci.* **22**, 559–566 (1965).
10. D. Tanré, M. Herman, and P. Y. Deschamps, "Influence of the background contribution upon space measurements of ground reflectance," *Appl. Opt.* **20**, 733–741 (1981).
11. P. N. Reinersman and K. L. Carder, "Monte Carlo simulations of the atmospheric point-spread function with an application to correction for adjacency effect," *Appl. Opt.* **34**, 4453–4471 (1995).
12. J. Dozier and J. Frew, "Atmospheric corrections to satellite radiometric data over rugged terrain," *Remote Sens. Environ.* **11**, 191–205 (1981).
13. ASTER (Advanced Spaceborne Thermal Emission and Reflection Radiometer) spectral library, NASA, <http://speclib.jpl.nasa.gov/>; cognizant scientist, simon.j.hook@jpl.nasa.gov.
14. R. Mc Clatchey, R. W. Fenn, J. E. A. Selby, F. E. Volz, and J. S. Garing, "Optical properties of the atmosphere," U.S. Air Force Cambridge Research Laboratory Rep. AFCRL-TR-71-0279, Environmental Research Paper 354 (U.S. AFCL, L. G. Hanscom Field, Bedford, Mass., 1971).
15. H. Cosnefroy, M. Leroy, and X. Briottet, "Selection and characterization of Saharan and Arabian desert sites for the calibration of optical satellite sensors," *Remote Sens. Environ.* **58**, 101–114 (1996).